SIMULATION OF STANDARDIZED WELDABILITY TESTS AND LINKAGE WITH FRACTURE AND FATIGUE BEHAVIOR

H. FU* and H. F. NIED*

** Mechanical Engineering and Mechanics, Lehigh University, Bethlehem, PA 18015, USA*
0000-0002-7668-0431, hfn2@lehigh.edu

DOI 10.3217/978-3-99161-089-2-027, license CC BY 4.0

ABSTRACT

This study examines the thermo-mechanical strains and stresses experienced by test specimens during weldability qualification tests, with a specific focus on the popular Varestraint and Houldcroft tests. These weldability tests are commonly used to identify critical thresholds for the initiation of hot cracking during the welding process, as well as subsequent crack propagation behavior in the presence of weld-induced residual stresses. The computational analysis in this study is primarily focused on the implementation of finite element models developed using ANSYS and SYSWELD software to simulate the coupled thermo-mechanical behavior during weldability tests. A notable aspect of the Varestraint weldability test is the application of a sudden external load during the welding process, introducing an additional external mechanical strain component in the test specimen. During this loading, the metal in the cooling weld pool is highly susceptible to fracture and is most likely to exhibit "hot cracking" behavior. To accurately determine the localized strains associated with this phenomenon, the finite element models used in this study employ element “birth” and “death” techniques, enabling precise tracking of strain and stress variations over time. This study attempts to accurately quantify the critical threshold strains for hot cracking initiation based on modified Brittleness Temperature Range (BTR) curves. Simulations of room-temperature fatigue crack propagation under the influence of combined welding residual stresses and external mechanical loads are also included. This is enabled by incorporating R-ratio crack growth rate effects in the simulations. Ultimately these simulations provide a more detailed and comprehensive understanding of the failure mechanisms in welded joints. An interesting fatigue crack growth example presented in this study is the numerical simulation of fatigue crack propagation in welded structures subjected to purely compressive external loading (compressive fatigue).

Keywords: Weld Fracture, Fatigue Crack Growth, R-Ratio, Residual Stress, Houldcroft Test, Varestraint Test, Hot Cracking, Brittleness Temperature Range, Compressive Fatigue.

INTRODUCTION

An important aspect of designing with welds in structural applications includes the anticipation of possible cracking during the welding process and/or subsequent cracking when the welded structure is subjected to external loads [1]. In addition to qualifying the welding metallurgy for specific welding applications, it is also important to accurately quantify the residual stresses that arise during welding and incorporate these stresses in the overall assessment of the likelihood of cracking and possible contribution to fatigue crack growth during service. Thus, it is not sufficient to simply consider the welding process in isolation, but for structural applications the weld design must also include a detailed stress analysis that includes a fracture assessment [1]. Fortunately, modern computational tools, e.g., finite element analysis (FEA), combined with significant improvements in computing power, have greatly improved the quality of large-scale numerical welding analyses for accurate structural stress and fatigue life analysis. Detailed fracture analysis can be linked with welding process simulations and conventional structural stress analysis to facilitate accurate predictions of fatigue crack growth behavior for critical structural applications.

There exist many historical structural failures that are directly attributed to cracking in welds, or cracking that originates in the Heat Affected Zone (HAZ) adjacent to the welds [1-2]. This cracking is usually attributed to metallurgical issues associated with the welding process and small cracks that are introduced into the highly stressed regions in, or adjacent to, the welds. Fig. 1 depicts an interesting example of an unusual structural failure that occurred in a bridge truss on the I-276 Delaware River Turnpike Bridge in New Jersey, USA, on a very cold day in December 2016. Fortunately, no one was injured when the heavy bridge truss suddenly fractured, but the bridge structure between the two supporting piers suddenly dropped approximately 5 cm and shifted loads to adjoining structural components that were not designed to carry this additional weight. In this case, weld filler metal had been used to "fill" improperly positioned bolt holes bored through the beam's flange during the bridge's construction. The fracture that severed the truss, initiated in a narrow zone between the weld filler metal and the boundary of the filled holes.

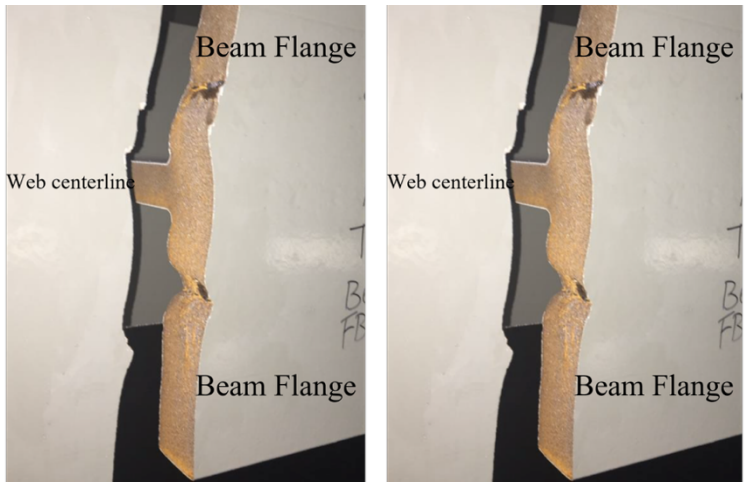

Fig. 1 Example of Fracture Initiated from the Boundary of Holes Filled with Weld Metal. I-276 Delaware River Turnpike Bridge Truss (2016) [3] [1]

Poor quality welds with slag inclusions introduced crack defects on the circumferential boundaries of the filled holes and because the circa 1950's high-carbon steel used in the bridge construction had a high fracture toughness transition temperature; the result was catastrophic fracture on a cold day.

In most weld related structural failures, crack growth occurs over a long period of time with the primary driving force being an external alternating load. Thus, small flaws that may be introduced during welding, grow in a subcritical manner (fatigue crack growth), until either being detected through Non-Destructive Testing (NDT), or upon reaching a critical length resulting in unstable fracture. Fig. 2 shows cross-section photos from controlled fatigue crack growth experiments conducted at the Fraunhofer-Institut für Werkstoffmechanik (IWM), Freiburg, on welded stiffener test specimens subjected to alternating bending [4]. As demonstrated by the semi-elliptic crack growth shown in Fig. 2, fatigue cracking originates at the toe of the fillet weld and propagates in a plane perpendicular to the maximum tensile bending stress. The rate of crack growth is dominated by the change in the stress intensity factor, ΔK , along the crack front due to the applied alternating bending. The residual stresses introduced by the fillet weld also play an important, but secondary, role in the fatigue crack growth behavior. Crack initiation usually occurs at the location of the highest combined local principal stress, in this case at the stress concentration located at the toe of the fillet weld. In carbon steel alloys, crack initiation is also closely associated with the formation of brittle Martensite phase in the HAZ.

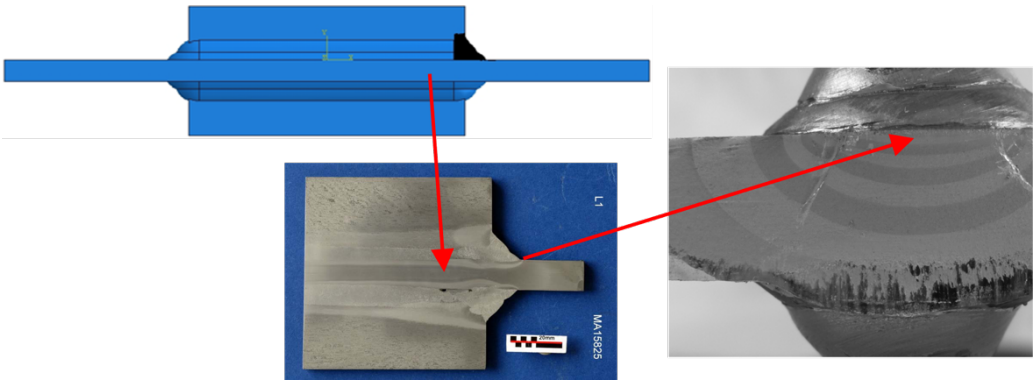

Fig. 2 Fraunhofer IWM Longitudinal Stiffener Test Specimen with Fatigue Crack Initiation at Weld Toe [4]

Cracking that occurs during the weld solidification process, at temperatures between the liquidus and solidus temperature, is often referred to as "hot cracking" (Fig. 3). The formation of cracks as the weld cools occurs because the strains in the deposited weld metal have exceed some critical strain necessary for the formation of cracks in the central portion of the weld. A variety of qualitative weldability tests have been developed and standardized over the years for assessing a material's susceptibility to solidification cracking. The two tests of particular interest in this study are the Trans-Varestraint test and the Houldcroft "Fishbone" test. These tests are usually conducted in a welding laboratory to help determine appropriate welding process parameters and compatible filler metals needed to avoid hot cracking. Unfortunately, since these standardized tests do not consider detailed information about the stress/strain state in the weld region itself, they can only provide a qualitative sense of the "susceptibility" of crack formation in the weld metal. For example, using the Varestraint test, the imposed external bending strain is usually used to calibrate cracking susceptibility as a function of temperature using a criterion like the Brittleness Temperature Range (BTR) methodology [6]. But the imposed bending strain is not the total strain in the weld metal, which also includes the significant thermomechanical strains that develop in the weld as it cools and solidifies.

Fig. 3 Example of Hot Cracking in a Fillet Weld [5]

As demonstrated in this paper, detailed welding simulations for these types of susceptibility tests, in conjunction with a critical strain criterion, e.g., the BTR methodology, provides a technique for developing quantitative tests that can provide the necessary data required for accurate prediction of crack initiation in structural welding applications. The BTR method can conveniently be used to define the critical strain values for weld metal cracking at different temperatures during solidification. The upper and lower temperature limits correspond to the weld metal's liquidus and solidus temperatures. As the temperature in the weld metal drops below its melting point and solidification begins, the strain-temperature relationship at specific points in the weld can be tracked. Comparison of the strain during solidification as a function of temperature with the critical strain obtained from an experimentally determined BTR curve, permits a quantitative assessment of the susceptibility of hot cracking for specific welding applications, i.e., if the strain at a given temperature exceeds the measured critical BTR strain, hot cracking will occur at that location in the weld.

Using modern computational techniques, it is feasible to: 1) accurately model the welding process and determine the local residual stress state in the neighborhood of the weld, 2) combine the welding residual stresses with complex external mechanical loading, and 3) accurately simulate 3-D fatigue crack growth based on postulated initial cracks starting from structural welds. As shown in this paper, this generally involves transferring intermediate welding stress results to finite element programs that can include external loading and efficient adaptive remeshing for the simulation of 3-D crack growth.

NUMERICAL SIMULATION OF VARESTRAINT AND HOULDCROFT TESTS

DESCRIPTION OF TRANS-VARESTRAINT TESTS

The two standardized weld cracking "susceptibility" tests modelled in this study are the Varestraint test and the Houldcroft "Fishbone" Test. The specific details associated with how these welding tests are conducted are described in many welding textbooks, e.g., [2]. The Varestraint hot cracking susceptibility test (Fig. 4) has two variations. The "regular" Varestraint test depicted in Fig. 4(a) uses a flat plate that is fixtured as a cantilever beam. The plate is suddenly bent to a specified radius of curvature on a bending block with a constant radius of curvature after the welding arc has reached the midpoint in the beam, as shown in Fig. 4(a). This causes an external mechanical bending strain component, acting parallel to the welding direction, that is accurately controlled by the radius of the Varestraint bending block. The key benefit of the Varestraint test is that the applied external strain can be easily controlled by using different radii bending blocks. The combination of the welding residual stresses during cooling and the external bending stress cause the formation of short cracks that are oriented perpendicular to the direction of motion of the weld arc.

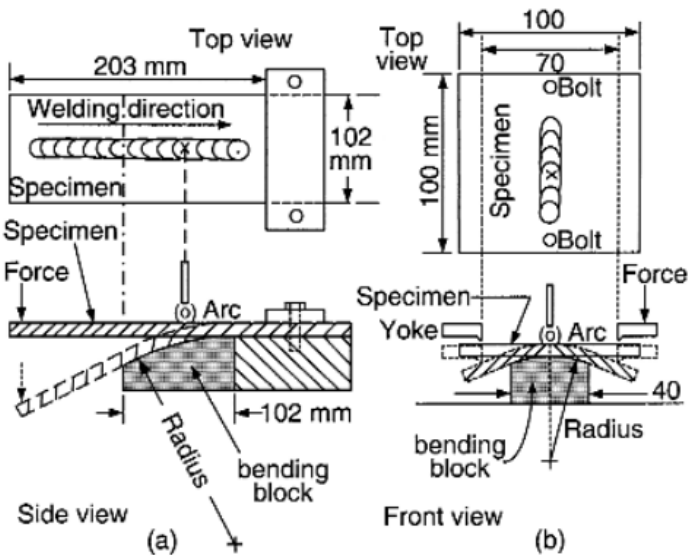

Fig. 4 (a) Schematic of the Two Different Varestraint Tests: (a) Cantilever Beam Bending, (b) Transverse Bending [2]

The closely related alternative Trans-Varestraint test (Fig. 4(b)), applies an external mechanical bending strain transverse to the welding direction along the entire length of the weld. In the Trans-Varestraint test, cracks will form parallel to the welding direction, replicating the hot cracking seen in fillet welds (Fig. 3) and the cracking that is observed in the Holdcroft test (Fig. 11b). Modelling either type of Varestraint test requires a simultaneous welding and mechanical bending simulation. This is shown schematically in Fig. 5 for a cantilevered Trans-Varestraint test, where a flat plate with an autogenous weld that starts at point C and ends at point A, is bent to a specified radius of curvature on a supporting bending block when the moving weld arc reaches the center of the plate at point B (Fig. 5(a)). This introduces a controlled bending strain perpendicular to the length of the cooling weld. The application of bending deformation during the welding simulation complicates the analysis, since the hot weld metal, which has a very low mechanical stiffness, is also subjected to very large mechanical strains.

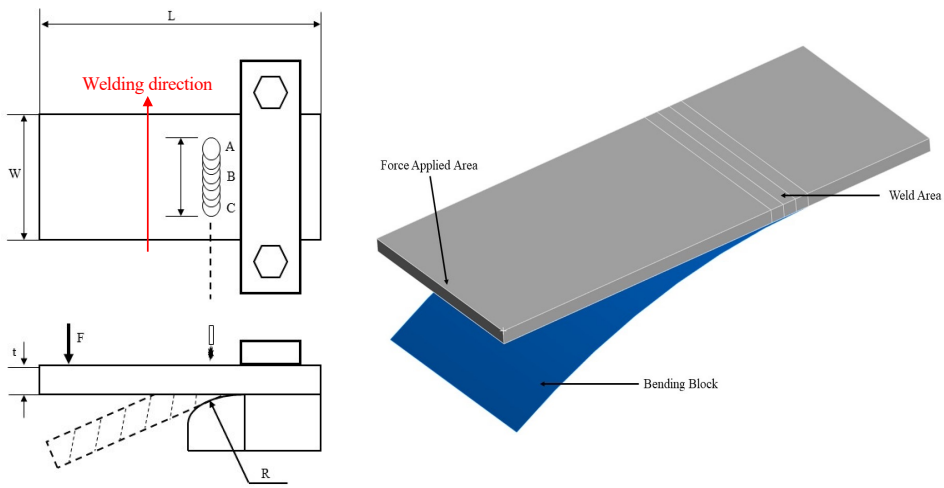

(a) (b)

Fig. 5 (a) Schematic of Cantilevered Transverse Varestraint Test Configuration and (b) FEA Model used for Analysis of Combined Welding Residual Stresses and External Mechanical Bending [7]

The mechanical strains in the portion of the weld at temperatures above the melt liquidus temperature, where the stresses are close to zero, play no role in crack initiation after the weld has cooled and begins to solidify. But the transverse surface displacements between points C and A, which can be quite large, will contribute to the concentrated total strain behind the moving heat source as the weld solidifies. The Trans-Varestraint test was modelled using a combined welding and bending simulation model [7] developed using ANSYS [8] with life/death option elements. This resulted in stable numerical calculations during the entire Varestraint welding simulation.

NUMERICAL SIMULATION OF TRANS-VARESTRAINT TESTS

Referring to Fig. 5(a), simulations of the Trans-Varestraint hot cracking susceptibility tests were performed on a plate with dimensions, L = 350 mm, W = 150 mm, t = 9 mm. Five different radii were used for the bending block: R = 4500 mm, 2250 mm, 1125 mm, 750 mm, 500 mm. Temperature dependent, rate independent, material properties for austenitic stainless steel (SS316) were used in the simulations. The relevant material properties are the thermal conductivity, specific heat, density, elastic modulus, coefficient of thermal expansion, and uniaxial yield strength. The thermomechanical properties of SS316 relevant for welding simulations with relatively rapid post-weld cooling are well-known and are readily available as a function of temperature, e.g., [9][9]. It should be noted that austenitic stainless-steel alloys do not exhibit the solid-state phase transformation volumetric strains observed in many other alloys, e.g., carbon steel. This simplifies the determination of the local strains for SS316.

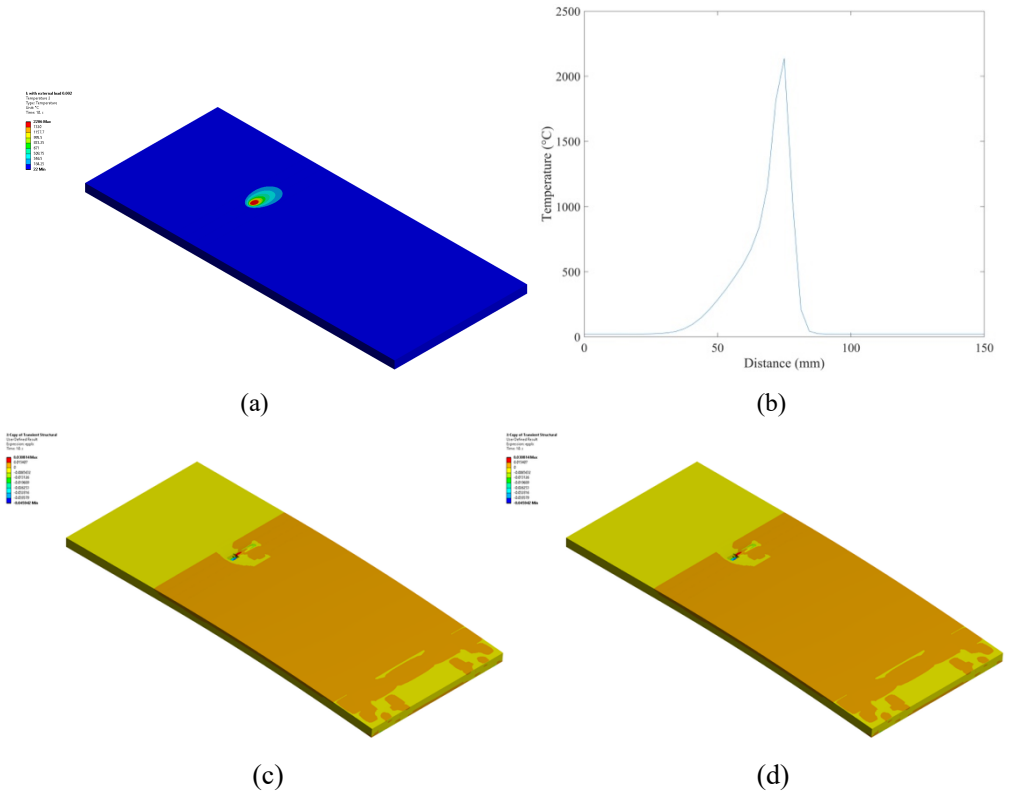

Fig. 6 Hot Cracking Simulations for Trans-Varestraint Test. (a) Temperature Contours for Moving Weld Arc at Center of Plate, (b) Temperature Distribution on Weld Line, (c) Mechanical Strain Introduced by Bending Deformation (R = 2250 mm), (d) Total Combined Welding and Bending Strains (R=2250 mm, Heat Input 1600 W, v=2.5 mm/s)

However, the solid-state phase transformation volumetric strains can be included in hot-cracking simulations for carbon steels if the relevant experimental data is available [9]-[10]. The ANSYS finite element model for the Trans-Varestraint test, which combines welding simulation with a suddenly applied external bending displacement, [7], is shown in Fig. 6. This mesh contains 16,560 elements with 178,368 nodes. Details concerning sensitivity of local strains to mesh refinement and time increment step size are given in [7]. Figs. 6(a)-(b) depict the temperature distribution during the welding process when the arc has reached the center of the plate based on a double-ellipsoid moving heat source with a heat input of 1600 W and welding velocity of 2.5 mm/s. The peak temperature in the weld attains a maximum temperature of 2206° C, which well exceeds the melting point of SS316 (T_m = 1400° C). Figs. 6(c)-(d) contain contour plots of the tensile strain distribution on the top surface of the Trans-Varestraint specimen perpendicular to the direction of the weld line. Fig. 6(c) depicts the mechanical bending strains acting on the weld line due to the deformation of the test specimen pressed against the radius bending block (R = 2250 mm). These are the strains that would typically be used for calibration of the Varestaint test, even though these strains do not incorporate any deformation behavior related to the welding process itself. The strain ε_{xx} perpendicular to the weld line in Fig. 6(c), due to plate bending around the R = 2250 mm radius bend block, has a maximum strain of $\varepsilon_{xx} = 1.9 \times 10^{-3}$ (~0.2% strain) in the central portion of the plate between points C and A (Fig. 5(a)). On either side of the plate outside of the $\mathrm{C} \rightarrow \mathrm{A}$ weld zone, the strain slightly decreases to $\varepsilon_{xx} = 1.6 \times 10^{-3}$. Fig. 6(d) shows the much more complex combined thermal and bending strains shortly after the application of the bending deformation during the welding simulation. As shown in Fig. 6(d), the combined strains are not symmetric because of the nonuniform thermal strains associated with the moving heat source.

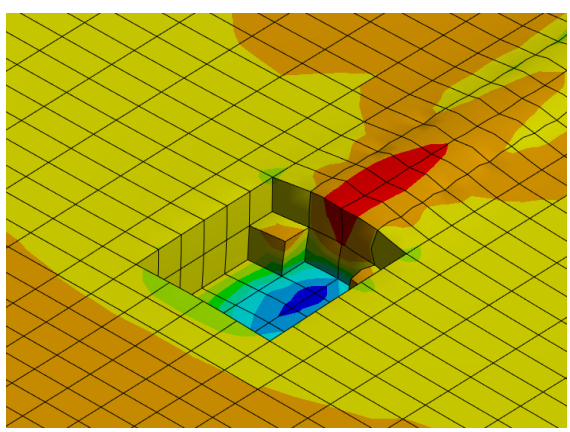

Fig. 7. Close-up View of Strain Contours from Fig. 6(d) with Elements Removed (Element Death Option) in the Portion of Melt Pool that Exceeds T_{m}

Fig. 7 shows a close-up view of the finite element mesh details around the moving heat source with the elements in the molten zone (element "death" option) removed for better visualization of the local strains around the double-ellipsoid moving heat source. As can be seen in Fig. 7, large combined total thermomechanical strains occur immediately behind the molten weld pool where weld solidification begins while subjected to the applied bending deformation. This strain concentration effect has been noted by other authors based on finite element simulations of the Trans-Varestraint test using other types of models [11]-[12].

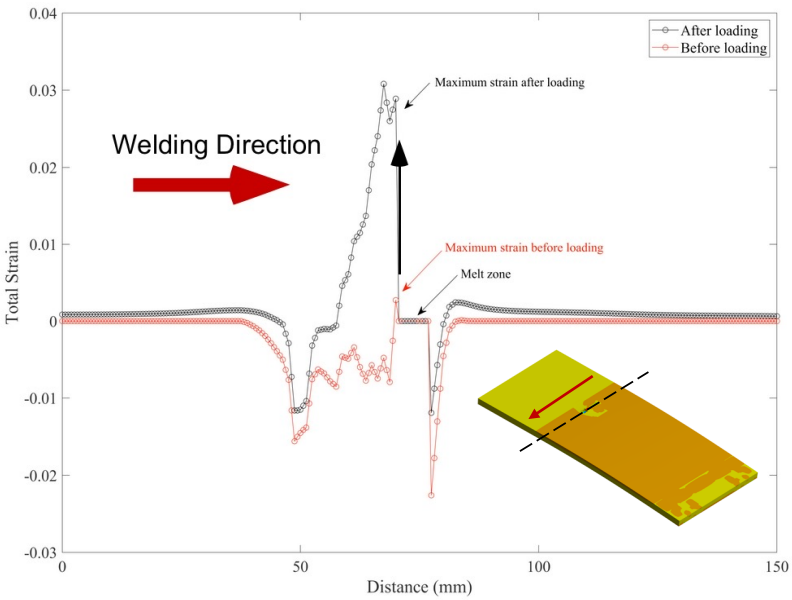

Fig. 8. Comparison of Welding and Mechanical Strains in Trans-Varestraint Test, Before and After the Application of the Bending Strain. Distance measured across the width of the plate (see Fig. 5(a))

Fig. 8 contains two plots that compare the total strain component perpendicular to the weld line across the entire width of the plate, just before, and after the application of the mechanical bending deformation. As can be seen in this figure, the thermal strains associated with the moving heat source are mostly compressive ahead of and behind the weld pool prior to the application of the bending displacements. Once the specimen is bent to the specified radius, the strains suddenly become tensile in the zone immediately behind the solidifying melt pool, due to a combination of the local tensile bending strain, the thermal strain associated with the cooling molten metal, and volumetric contraction during solidification. As shown in Fig. 8, the maximum total strain immediately behind the weld pool reaches a value of approximately $\varepsilon_{xx} = 0.03$, which exceeds the combined estimate for the local mechanical strain ($\varepsilon_{xx} = 0.002$)

and the thermal strain ($\varepsilon_{xx} = 0.0028$) by approximately a factor of 6x. This indicates that the total strain in the region immediately behind the cooling weld pool is dominated by the coupled thermomechanical strain and the volumetric strain associated with the phase change from the liquid to the solid state. This behavior in the local strains associated with the Varestraint test was also noted in [11]-[12]. As the weld continues to cool and solidify in the region behind the moving heat source, the total strain rapidly decreases, while the tensile residual stresses in the wake of the heat source significantly increases.

Repeating the above Trans-Varestraint simulations, using the same welding parameters, but varying the radii of curvature of the Varestraint bend block permits the construction of an "updated" BTR curve based on the original experimental BTR curve generated in [6], which only considered the specified mechanical bending strain. Fig. 9 provides a comparison between the original BTR curve obtained from [6] with a modified BTR curve generated in this study. Due to the inclusion of the local strains computed from the complete welding model, there is a significant upward shift in the critical strain as a function of temperature in the modified BTR curve. It is believed that the updated BTR curve provides a more accurate representation of the critical strain necessary for hot cracking that can then be used for the prediction of hot cracking using other welding process parameters and geometries – a conclusion also given by other authors [11]-[12]. This will be demonstrated for hot cracking predictions in Houldcroft test specimens.

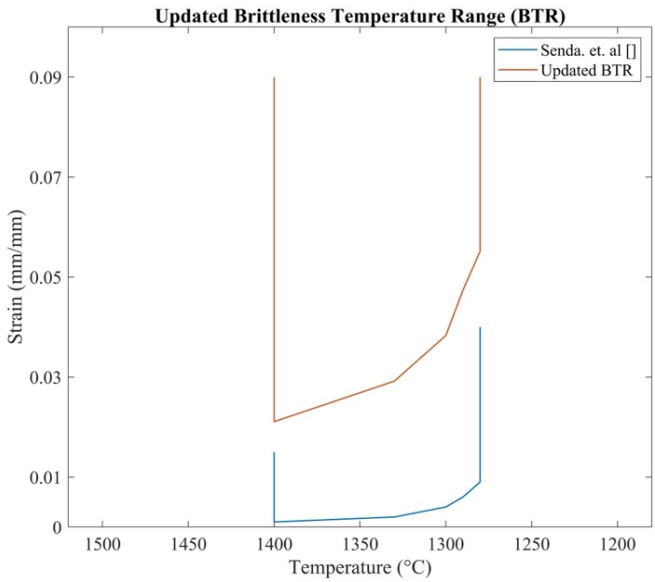

Fig. 10. Conventional BTR Curve (lower curve) Based on Mechanically Applied Bending Strains Only [6] and Comparison with Updated BTR Curve (upper curve) that Includes Total Welding Strains and Externally Applied Mechanical Bending

DESCRIPTION OF HOULDCROFT TESTS

Fig. 11(a) shows the typical geometry of the Houldcroft Test. In the Houldcroft test, vertical slots are cut into a rectangular plate so that there is a variable degree of transverse constraint acting on the weld as it cools. If the constraint is great enough, then cracking will initiate in the region with the greatest constraint (between the smallest slots) and crack arrest will occur when the transverse constraint is insufficient to cause further crack growth (between longer slots).

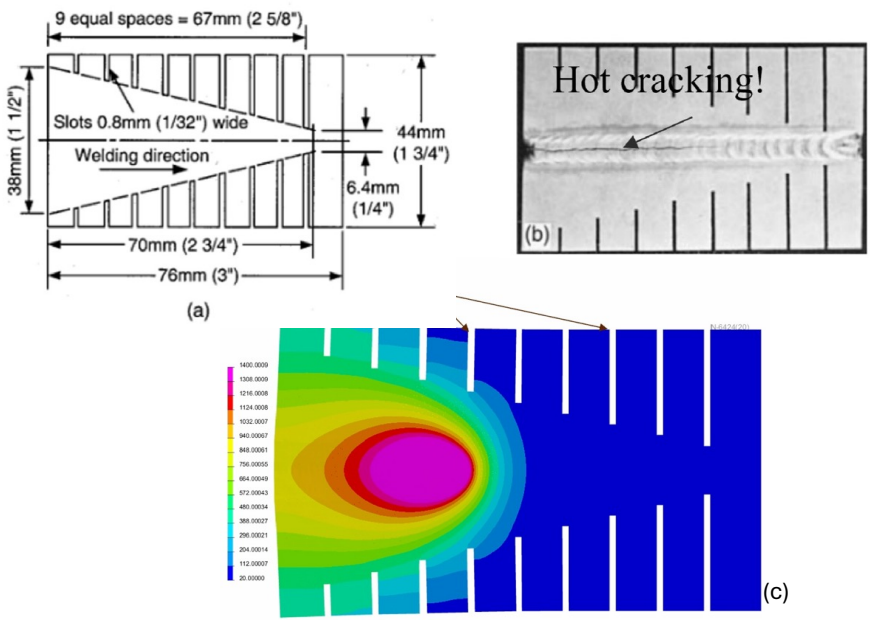

Fig. 11. (a) Schematic of Houldcroft "Fishbone" Test [2]. (b) Hot Cracking during Test [2]. (c) Welding Simulation of Houldcroft Test [7] using SYSWELD [9].

An example of hot cracking that can occur during a typical Houldcroft test is shown in Fig. 11(b). The numerical simulation of the Houldcroft test begins with the 3-D transient heat transfer simulation of the moving weld arc as shown in Fig. 11(c). In this study, the Houldcroft simulations were conducted using the FEA weld simulation software SYSWELD [9], [9]. Once the heat transfer calculation is completed, a full thermomechanical stress analysis provides the strains and residual stresses that are responsible for the initiation and propagation of horizontal cracks in the weld.

NUMERICAL SIMULATION OF HOULDCROFT TESTS

Welding simulations of the Houldcroft susceptibility test were performed using the same material properties, austenitic stainless steel (SS316), that were used for simulating the Trans-Varestraint test. Fig. 12(a) depicts the Houldcroft plate geometry and Fig. 12(b) the

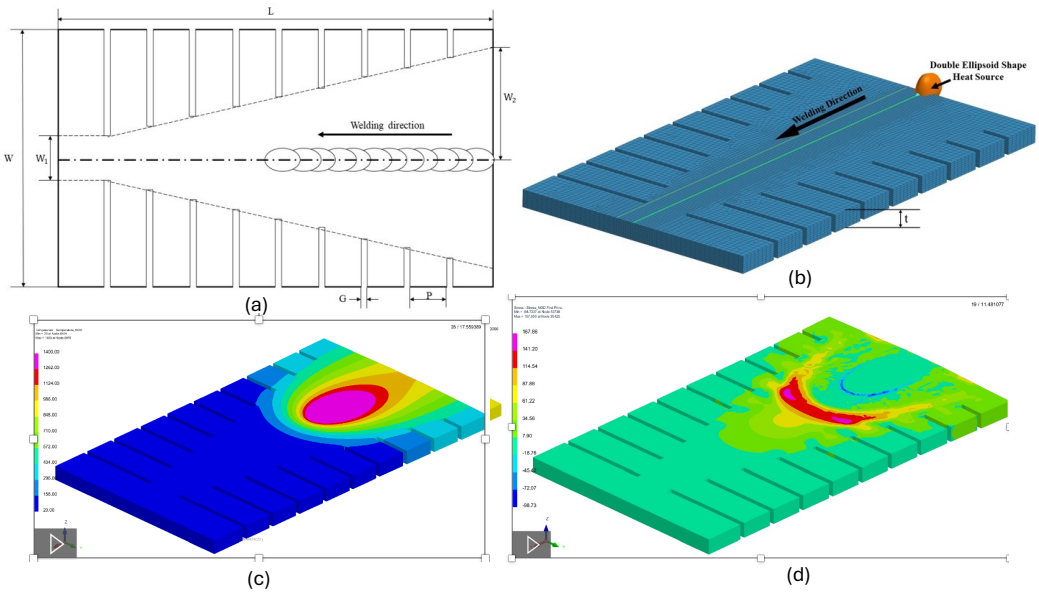

Fig. 12. FEA Simulation of the Holdcroft Test. (a) Geometry, (b) SYSWELD Mesh, (c) Temperature Contours, (d) First Principal Stress Contours

Table 1. Houldcroft Plate Dimensions (referring to Fig. 12)

	W	**W_1**	**W_2**	**L**	**G**	**P**	**t**
(mm)	44.6	7.72	38.78	76	1	6.5	3

Table 2. Constant Power Welding Heat Source for Houldcroft Test Simulations

	Constant Heat Input (1650 W)	
	Heat input per unit length (J/mm)	Welding speed (mm/s)
Case1	1850	0.893
Case2	1232	1.340
Case3	924	1.787

3=D finite element mesh. The plate geometric dimensions are given in Table 1. Three welding simulations with welding velocities and heat input per unit length (J/mm) used in the double ellipsoid heat source model, resulting in a constant heat input (W) are given in Table 2. In the 3-D SYSWELD model shown in Fig. 12 there are 65,196 elements and 75,178 nodes. Convective and radiative heat transfer boundary conditions were specified to simulate cooling in air. Fig. 12(c) shows the temperature contours for the moving heat source during an autogenous welding simulation, and Fig. 12(d) shows a typical principal stress contour.

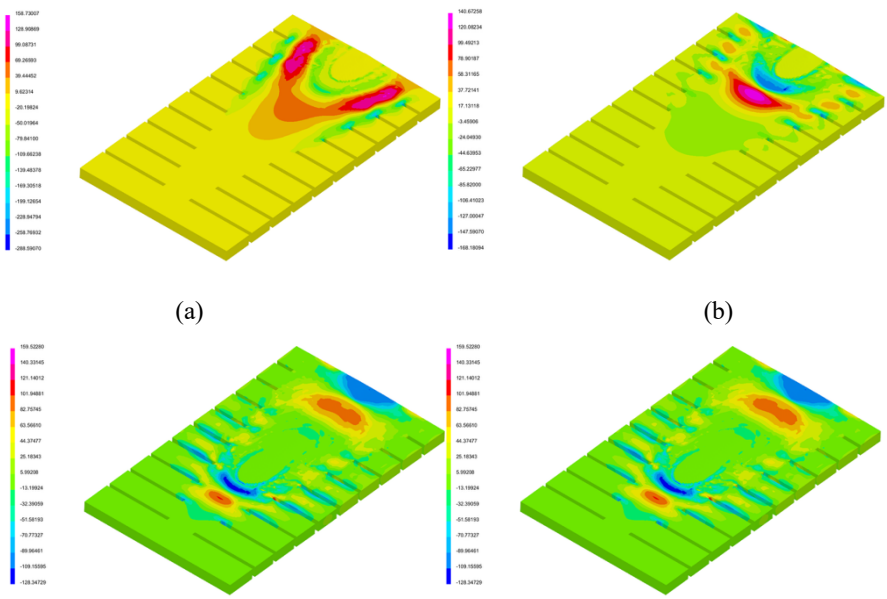

(a) (b)

(c) (d)

Fig. 13. Welding Stresses in Holdcroft Test Configuration – Case 1. (a) Longitudinal Stress at t=5s, (b) Transverse Stress at t= 5s, (c) Longitudinal Stress at t=24s, (d) Transverse Stress at t=24s

Fig. 13 shows the contours for the longitudinal and transverse stress components during the Holdcroft welding simulation at two different times as the weld arc moves along the surface

of the plate. The strains at any specific point on the plate surface can be plotted as a function of time and temperature. For the three constant power input cases (1650 W) given in Table 2, the transverse strains as a function of time at a selected point 3.13 mm from the edge of the plate are shown in Fig. 14. By plotting the temperature vs strain on the modified BTR curve previously generated using the Trans-Varestraint simulation, it is possible to make hot cracking predictions in the Holdcroft test configuration. It is interesting to note that only Case 2, with a welding velocity of 1.340 mm/s, clearly falls into the hot cracking range as predicted by the BTR curve, i.e., for the constant heat input welding arc models, welding at a lower or higher velocities does not seem to be as likely to exhibit hot cracking behavior as the intermediate Case 2 velocity.

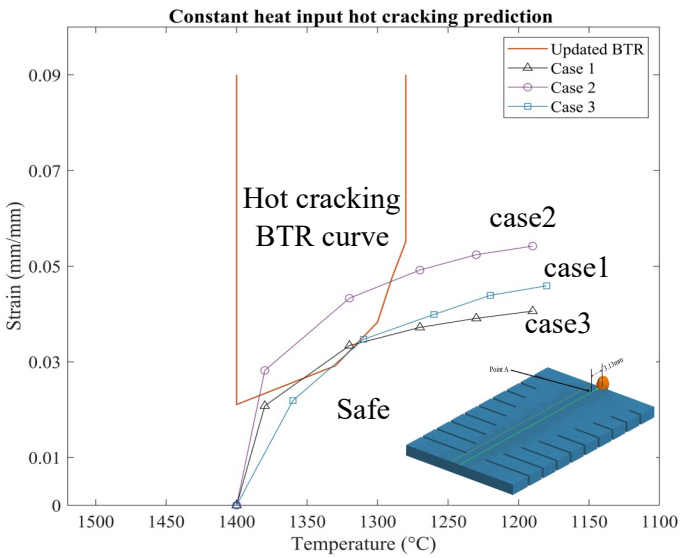

Fig. 14. Hot Cracking Susceptibility Predictions for Three Houldcroft Tests based on Modified BTR Curve and Constant Heat Input Weld Arc. Strains at Point A (x = 3.13 mm) as a Function of Temperature

COMBINED WELDING AND FRACTURE SIMULATIONS

Once it is postulated that cracking may occur during welding, e.g., as predicted by the weld susceptibility tests described above, or if a fracture assessment is to be made based on crack initiation in locations of high stress concentrations, as depicted in Figs. 1 and 2, a 3-D fatigue crack propagation simulation can be performed. Fatigue crack propagation analysis can be used to provide a reasonable remaining life estimate based on experimentally measured fatigue crack growth rate data. The propagation of three-dimensional cracks should be performed considering both the external alternating loads as well as the welding residual stresses. In this

study, an example residual stress distribution is obtained for the SS316 fillet welded T-joint shown in Fig. 15(a), with the dimensions given in Table 3. The T-joint welding model was simulated in SYSWELD [9] to obtain the temperatures (Fig. 15(b)) and the welding residual stress distributions (Fig. 16) used as input for the fatigue crack growth simulation. For the fillet welded T-joint model shown in Fig. 15, there are 14,650 elements with 17,476 nodes. In the welding model, the heat input per unit length is specified to be 550 J/mm with the welding velocity given as 3 mm/s.

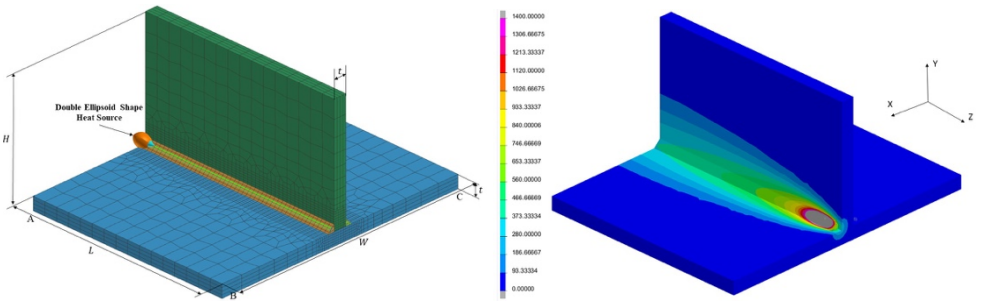

(a) (b)

Fig. 1. (a) SYSWELD Finite Element Model with Dimensions and Boundary Conditions for Welded T-Joint. (b) Temperature Distribution Towards the End of the First Weld Pass

Table 3. Fillet Welded T-Joint Dimensions

	H	**L**	**W**	**t**
(mm)	60	96	120	6

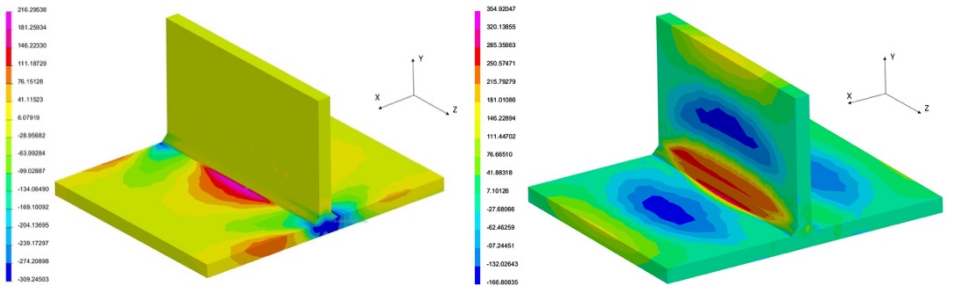

(a) (b)

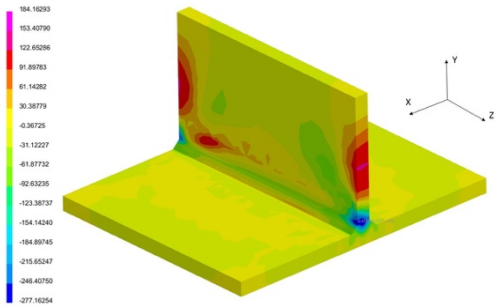

(c)

Fig. 16. Welding Residual Stresses for T-Joint with Fillet Welds. (a) Stress Component in x-direction Transverse to Weld, (b) Longitudinal Stresses, (c) Stresses in vertical direction

The stress contour plots shown in Fig. 16 contain the residual stresses in the three orthogonal directions after the welded T-joint has cooled down to room temperature.

To prepare the crack growth simulation model, two locations at the toe of the 1st fillet weld were chosen to simulate crack growth from small (2 mm radius) semicircular surface cracks subjected to both the welding residual stresses and an external alternating load. These locations are shown in Fig. 17(a), with one surface crack, Crack1, located at the highest stressed region in the central portion of the plate and another surface crack, Crack2, located at a relatively low stressed region at the fillet weld toe where there is a gradient in the transverse residual stress that will result in nonsymmetric crack growth.

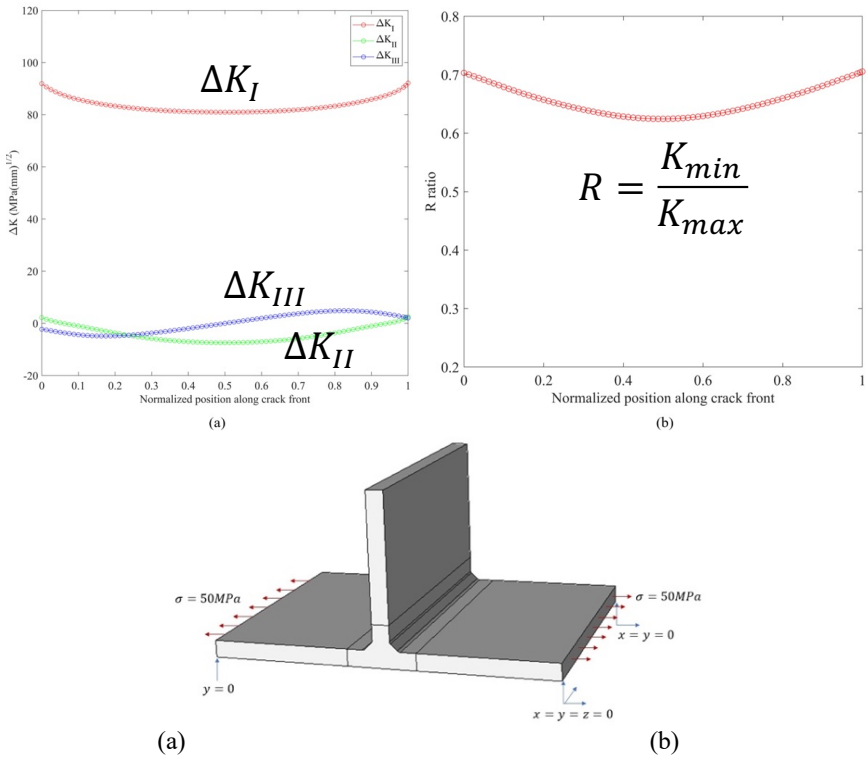

Fig. 17. (a) Selected Location for Placement of 2 mm Radius Semicircular Surface Cracks at Fillet Weld Toe. (b) Alternating External Loads, (0, +50 MPa, 0) for Fatigue Crack Growth

For simulation of 3-D crack growth, the residual stresses from the SYSWELD welding model shown in Fig. 16 are mapped to a different, more refined, finite element mesh generated using the automatic meshing program SimModeler [13]. Details concerning mapping of the SYSWELD generated residual stresses to a refined ANSYS mesh containing the embedded crack geometry, suitable for fracture analysis using SimModeler, are given in [7]. These mapped stresses can then be used as "initial" stresses in an ANSYS fracture calculation with the additional external loading boundary conditions shown in Fig. 17(b). The SimModeler meshing software permits the insertion of a surface crack geometry at specific locations in the original uncracked geometry and also automatically generates a highly refined "tunnel" mesh around the crack tip suitable for use in an ANSYS FEA model for the calculation of the stress intensity factors along the crack front. As the crack propagates in fatigue, the geometry changes and the finite element mesh is adaptively remeshed using the SimModeler meshing software. An alternating external (0, +50 MPa, 0) load as shown in Fig. 17(b), applied horizontally to the T-joint flange, provided the external fatigue loading for the simulation of fatigue crack growth in the presence of the existing welding residual stresses.

Incremental simulation of the directional crack growth in this study is based on the maximum circumferential stress criteria [14] where the crack front is advanced in a direction

perpendicular to the maximum local circumferential stress at the crack tip. The local maximum circumferential stress can be determined from the asymptotic crack tip stresses and is expressed in terms of the mixed-mode stress intensity factors K_I and K_{II} at any position along the crack front. Assuming that the critical principal stress for crack advance under mixed-mode conditions is identical to the critical stress necessary for crack growth under mode I conditions, the angle for crack advance θ_P can be determined from [14],

$$\left(\tan\frac{\theta_p}{2}\right)_{1,2} = \frac{1}{4}\frac{K_I}{K_{II}} \mp \frac{1}{4}\sqrt{\left(\frac{K_I}{K_{II}}\right)^2 + 8} \quad . \tag{1}$$

In (1), for $K_{II} > 0$, the negative sign is taken on the square root term and when $K_{II} < 0$ the sign is positive.

To properly simulate fatigue crack growth (FCG) under the influence of welding residual stresses, a fatigue crack growth rate law that incorporates the effect of the static residual stresses should include the R-ratio in the crack growth rate behavior. For this study, the Walker equation [15] given by

$$\frac{da}{dN} = C\left(\frac{\Delta K_{eq}}{(1-R)^{1-m}}\right)^n , \tag{2}$$

where a is he crack length and N is the number of alternating load cycles, provides a simple crack growth rate relationship with the R-ratio given by

$$R = \frac{K_{\min}}{K_{\max}} \quad . \tag{3}$$

In (2), the equivalent stress intensity factor K_{eq} is defined as

$$K_{eq} = \sqrt{\left(K_I\cos^3\frac{\theta_p}{2} - 3K_{II}\cos^2\frac{\theta_p}{2}\sin\frac{\theta_p}{2}\right)^2 + \frac{K_{III}^2}{(1-\nu)}} \quad , \tag{4}$$

$$\Delta K_{eq} = K_{eq}^{\max} - K_{eq}^{\min} \quad , \tag{5}$$

$$K_{\min} = K_{RS} - K_L \, , \qquad K_{\max} = K_{RS} + K_L \quad . \tag{6}$$

In the above equations, $K_{\min}$ is the minimum stress intensity factor, $K_{\max}$ the maximum stress intensity factor, K_{RS} the stress intensity factor due to the residual stresses, K_L is the stress intensity factor caused by cyclic external loads, and ν is Poisson's ratio. For SS316 the

empirical constants used in the Walker equation (2) were adopted from [15] and are given by $n = 3.159$, $m = 0.32922$, and $C = 1.67154 \times 10^{-13}$ (mm/cycle)·((MPa·√mm)/(1-R)$^{0.67078}$)$^{-3.159}$.

Fig. 18 shows example fatigue crack growth simulation results for Crack1 subjected to the welding residual stresses located in the center of the plate flange, at the edge of the fillet weld toe, as shown in Fig. 17(a), with the alternating external loading shown in Fig. 17(b). In this case, the crack growth simulation continues until the crack grows to a depth of 4.75 mm after N = 20,657 cycles. Fig. 18(b) also contains a side view showing the plane of the crack and Fig. 18(c) shows the initial change in the stress intensity factors along the 3-D semicircular crack front at the beginning of the fatigue crack growth. As can be seen, the crack is dominated by the Δ change in the mode I stress intensity factor, which causes the crack to grow in a smooth planar manner.

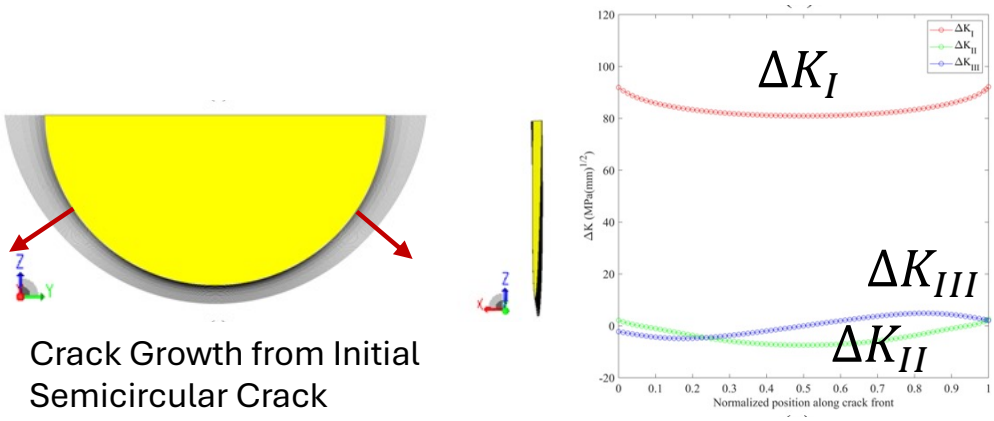

Fig. 18. (a) Close-up View of Fatigue Crack1 Simulation Results for Crack Located at Weld Toe using Walker equation, (b) Side View of Crack Growth Plane, (c) Initial Changes in the Stress Intensity Factors Along Semicircular Crack Front due to Alternating External Loading

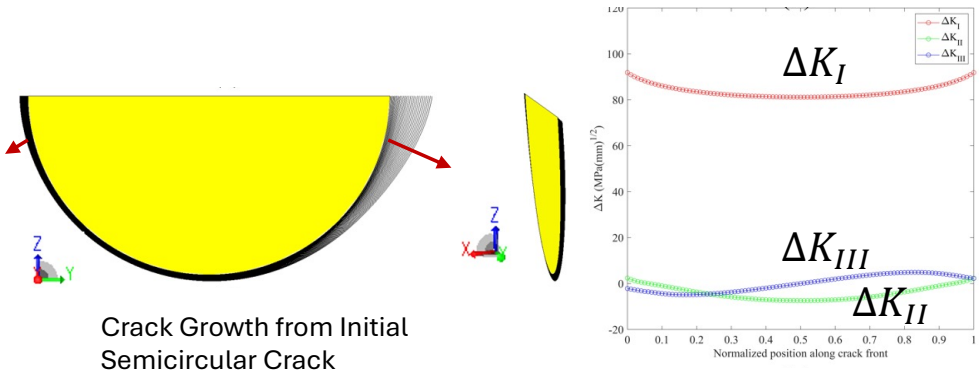

(a) (b) (c)

Fig. 19. a) Fatigue Crack2 Simulation Results for Crack Located at Weld Toe using Walker equation showing Uneven Crack Growth, (b) Side View of Crack Growth Plane, (c) Initial Changes in the Stress Intensity Factors Along Semicircular Crack Front due to Alternating External Loading

Fig. 19 shows the crack growth behavior for the initially semicircular surface crack, Crack2, inserted into the location where there is a much smaller residual stress, but there is a strong stress gradient in the welding residual stresses in the plane of the crack. Since the Walker equation takes into account the influence of the stress ratio *R*, the crack will grow in an uneven manner as depicted in Fig. 19(a), with the more rapid crack growth occurring on the side of the crack subjected to the higher tensile residual stress (see Fig. 17(a)). To attain the crack shape shown in Fig. 19(a), required a much larger number of load cycles, N = 272,968, than for the crack located in the high residual stress region shown in Fig. 18. The nonsymmetry in the crack growth behavior is due to the variation in the R-ratio along the crack front and can be entirely attributed to the welding residual stresses. In this figure, the maximum R-ratio occurs at the right end of the crack front in Fig. 19(a), resulting in faster fatigue crack growth at this end of the crack front. The side view of the crack front shown Fig 19(b) shows that the propagating crack still remains planar. Fig. 19(c) contains the change in the stress intensity factors along the initial semicircular crack front at the beginning of the fatigue simulation. As expected, the change in the stress intensity factors are essentially identical to the stress intensity factors for the crack located in the region with the higher welding residual stresses. This is because the alternating external load, which is identical for both cracks, provides the dominant crack driving force. Though the welding residual stresses play a secondary role in the fatigue crack propagation rates through the R-ratio, it is still the welding residual stresses, in combination with local stress concentration effects, that determines the location of where cracking will initiate.

An interesting and somewhat unusual fatigue crack growth problem can occur in welded structures subjected to only compressive external loading [16]. An example simulation of this phenomenon is demonstrated using the external loading shown in Fig. 20.

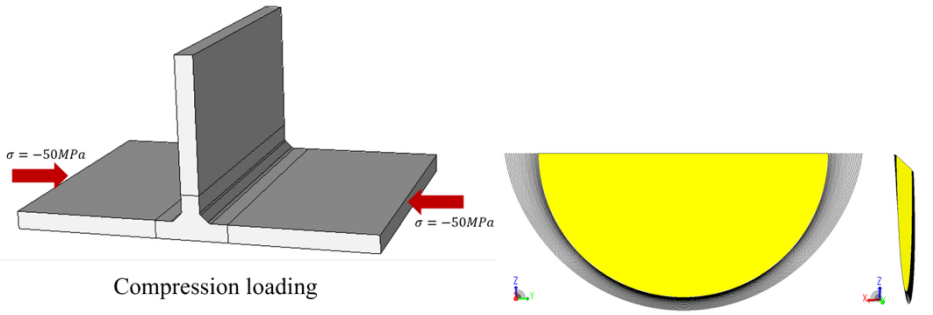

Fig. 20. Fatigue Crack Growth for Initial (2 mm radius) Semicircular Surface Crack (Crack1) at Weld Toe Subjected to Alternating Compressive Loads

In this example, the flanges of the T-Joint are loaded in uniform cyclic compression (-50 MPa, 0, -50 MPa). In the absence of any residual stresses, preexisting cracks would not be expected to grow in fatigue. However, in the region of the fillet weld with the tensile residual stresses shown in Fig. 17(a), cracks, e.g., Crack1, will experience a positive ΔK on each load cycle when the -50 MPa load is released. Thus, incremental crack growth will occur every time the flange plate is unloaded. The resulting crack growth behavior is depicted in Fig. 20, where the fatigue crack growth was simulated using the Walker crack growth rate law (2). For the semicircular crack to attain the shape shown in Fig. 20 required N = 47, 041 cycles, more than double the number of cycles needed to obtain approximately the same crack growth (Fig. 18(a)) when the T-Joint is subjected to positive alternating load cycles of the same magnitude.

Fig. 21 contains plots of the positive changes in the stress intensity factors for the compressive alternating loading shown in Fig. 20. The positive ΔK due to unloading is essentially identical to the positive ΔK that occurs for the tensile alternating external loading shown in Fig. 18.

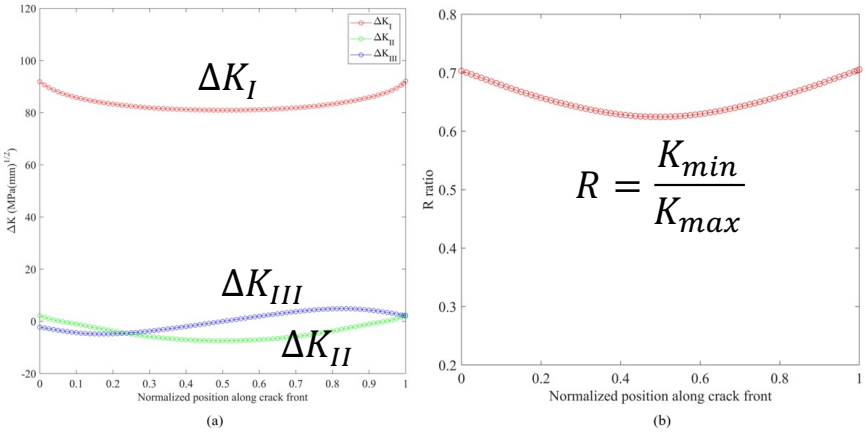

Fig. 21. (a) Initial Changes in Stress Intensity Factors Along Crack Front due to Alternating Compressive Loading and Welding Residual Stresses, (b) R-Ratio Along Crack Front

CONCLUSIONS

Two different types of cracking phenomena were investigated in this paper. The first type of cracking behavior is related to the hot cracking susceptibility tests that are routinely conducted when qualifying new welding processes and determining the weldability of new metallurgical alloys. The detailed numerical simulations presented in this paper demonstrate the feasibility of accurately determining the highly localized strain concentrations that occur at the trailing edge of the cooling weld pool in the Trans-Varistraint test and use welding simulations to update existing BTR curves for improved hot cracking predictions in structural welding applications. Application of this methodology allows one to use the qualitative Trans-Varistraint test results in a quantitative manner for making hot cracking predictions in welding applications with entirely different conditions than the Trans-Varistraint test. An example of this is given for predictions of hot cracking in the Houldcroft test configuration.

The second type of cracking behavior examined in this paper is associated with the modelling of fatigue crack growth behavior in welded structural components. The methodology for incorporating the static welding residual stresses is demonstrated by first obtaining the welding residual stresses using a dedicated FEA welding simulation software package (SYSWELD). Then “mapping” the resulting residual stresses to a finite element program more suitable for detailed crack growth analysis (ANSYS). This is facilitated by using specialized meshing software (SimModeler) that generates adaptive meshes for growing fatigue cracks in the presence of welding residual stresses. The welding residual stresses contribute primarily to fatigue crack growth through the R-ratio effect. Inclusion of R-Ratio effects is of importance in the assessment of fatigue fracture behavior for welded structures. It is demonstrated in this paper that fatigue crack growth, which incorporates the contribution of the welding residual stresses, can be efficiently performed for critical structural

applications. This is demonstrated by the interesting example of compressive fatigue, where crack growth is possible due to the application of cyclic compressive loading only because of the presence of internal welding residual stresses.

ACKNOWLEDGEMENTS

The authors gratefully acknowledge the academic licenses and software provided by ANSYS, ESI (SYSWELD) and Simmetrix, Inc. (SimModeler) used to develop the simulation models in this study. The authors would like to specifically express their appreciation for the technical assistance provided by Mr. R. Silva (ESI, Inc.) and Dr. A. Loghin (Simmetrix, Inc.).

REFERENCES

[1] K. MASUBUCHI: *Analysis of Welded Structures*, Pergamon Press, 1980.
[2] S. KOU: *Welding Metallurgy*, 2nd ed., Wiley-Interscience, 2002.
[3] J. DUPONT, H. NIED, R. SAUSE: 'Material Testing and Fracture Analysis of a Truss Cord Member from the NJTA/PTC Delaware River Bridge (Phase 2), Final Report', *ATLSS* No. 17-08, 2017.
[4] H. NIED, D. SIEGELE: 'Study of the Influence of Material and Welding Modeling on the Residual Stresses in Longitudinal Stiffeners', *66th Annual Assembly and International* 19 *Conference, Commission XIII Fatigue of Welded Components and Structures*, Doc. XIII-2479-13, International Institute of Welding, Essen, Germany, Sept. 11-15, 2013.
[5] P. NANAVATI: 'Cracking in the Weld Joint Between X2CrNi12 and CS Joints using E3098L Filler?', *Welding Metallurgy Articles*, https://weldingknowledge.co.in/2021/02/17/cracking-in-the-weld-joint-between-x2crni12-and-cs-joints-using-e309l-filler/, 2021.
[6] T. SENDA, F. MATSUDA, G. TAKANO, K. WATANABE, T. KOBAYASHI, T. MATSUZAKA: 'Fundamental Investigations on Solidification Crack Susceptibility for Weld Metals with Trans-Varestraint Test', *Transactions of the Japan Welding Society,* 2, 2, 45-66, 1971.
[7] H. FU: 'Simulation of 3-D Crack Growth in Welded Structures based on Residual Stresses Obtained from Detailed Welding Process Models'*, Ph.D. Dissertation*, Lehigh University, 2025.
[8] ANSYS, Version 12.0 Ansys Inc. Canonsburg, PA, USA, 2009.
[9] SYSWELD 2021.0 – Documentation Package, ESI North America, Farmington Hills, MI, 2021.
[10] A. ALRUMAYH, H. NIED: 'Simulation of Residual Stresses During the Wire Arc Additive Manufacturing (WAAM) Process', *Mathematical Modelling of Weld Phenomena 13*, Verlag der Technischen Universität Graz, pp. 283-303, 2023.
[11] Y. WEI, Z. DONG, R. LIU, Z. DONG: 'Modeling the Trans-Varestraint Test with Finite Element Method', Comp. Mat. Sci., 35, 84-91, 2006.
[12] S. MAEDA, W. WANG, M. HABATA, K. IKUSHIMA, M. SHIBAHARA: 'Mechanical Study of Trans-Varestraint Test by Using Numerical Analysis of Cracking Based on Idealized Explicit FEM ', Quarterly J. of the Japan Welding Society, 41, 2, 21s-25s, 2023.
[13] SIMMETRIX INC, SimModeler Crack 11.0, Installation, User Guide Release Notes, 10 Executive Park Drive, Clifton Park, NY 12065 USA.
[14] F. ERDOGAN, G. C. SIH: 'On the Crack Extension in Plates Under Plane Loading and Transverse Shear', J. Basic Eng., 85(4), 519-525, 1963.
[15] R. J. SANFORD: Principles of Fracture Mechanics, Prentice Hall, 2003.

[16] D. MALSCHAERT, M. VELJKOVIC, J. MALJAARS: 'Numerical Simulations of Residual Stress Formation and Ist Effect on Fatigue Crack Propagation in a Fillet Welded T-Joint', *Eng. Frac. Mech.*, 306, 2024.